Available online at www.sciencedirect.com
ScienceDirect
Journal of Nuclear Materials 363–365 (2007) 365–370
journal of nuclear materials
www.elsevier.com/locate/jnucmat

Improved radiation measurements on JET – First results from an upgraded bolometer system

A. Huber [a,*], K. McCormick [b], P. Andrew [c], M.R. de Baar [d], P. Beaumont [c], S. Dalley [c], J. Fink [b], J.C. Fuchs [b], K. Fullard [c], W. Fundamenski [c], L.C. Ingesson [d], G. Kirnev [c], P. Lomas [c], F. Mast [b], S. Jachmich [a], G.F. Matthews [c], Ph. Mertens [a], A. Meigs [c], V. Philipps [a], J. Rapp [a], G. Saibene [e], S. Sanders [c], R. Sartori [e], M.F. Stamp [c], W. Zeidner [b], JET-EFDA Contributors [1]

[a] *Institut für Plasmaphysik, Forschungszentrum Jülich GmbH, EURATOM Association, Trilateral Euregio Cluster, D-52425 Jülich, Germany*
[b] *Max-Planck-Institut für Plasmaphysik, EURATOM Association, 85748 Garching, Germany*
[c] *Euratom/UKAEA Fusion Association, Culham Science Centre, Abingdon, Oxon OX14 3DB, UK*
[d] *FOM-Instituut voor Plasmafysica, Nieuwegein, The Netherlands*
[e] *EFDA Close Support Unit – Garching, Boltzmannstrasse 2, D-85748 Garching, Germany*

Abstract

To improve the quality of radiation measurements, two new bolometric cameras with horizontal and vertical views of the plasma cross-section have been installed on JET. These cameras provide measurements with significantly improved spatial resolution, allowing the divertor and main chamber radiation fractions to be clearly resolved. Analysis of radiation profiles under attached and detached divertor conditions as well during the formation of an X-point MARFE (XPM) close to an ohmic density limit are presented. The radiation power fraction $\gamma = P_{\mathrm{rad}}/P_{\mathrm{heat}}$ increases from 0.5 to 0.8 just before XPM onset. A large fraction of this radiation is located in the divertor ($P^{\mathrm{div}}_{\mathrm{rad}}/P^{\mathrm{tot}}_{\mathrm{rad}} = 0.56$ at low density and about 0.67 at XPM onset). In addition, spatial distributions of radiation in recent ITER-like configuration discharges are presented.

PACS: 52.40.Hf; 52.25.Vy; 52.55.Fa

Keywords: Bolometer tomography; Density limit; Divertor radiation; Detachment; Divertor asymmetry

1. Introduction

Partially detached divertor operation is mandatory to reduce strike point power fluxes in long pulse, high power fusion devices. Our understanding of this complex detached state is still incomplete

* Corresponding author. Fax: +49 2461 61 2660.
E-mail address: a.huber@fz-juelich.de (A. Huber).
URLs: www.fz-juelich.de/ipp (A. Huber), www.fz-juelich.de/ipp (S. Jachmich), www.fz-juelich.de/ipp (Ph. Mertens), www.fz-juelich.de/ipp (V. Philipps), www.fz-juelich.de/ipp (J. Rapp).
[1] See the Appendix of J. Pamela et al., Fusion Energy 2004 (Proceedings of the 20th International Conference, Villamoura, 2004) IAEA, Vienna (2004).

0022-3115/$ - see front matter © 2007 Elsevier B.V. All rights reserved.
doi:10.1016/j.jnucmat.2007.01.124

and requires 2D simulations which themselves rely on high quality experimental data to be properly constrained. The radiation distribution is particularly important, but is often poorly resolved in space and magnitude in the divertor region where it is most required.

In this paper, we describe ohmic and L-mode density limit discharges using JET's new improved diagnostics. In addition, the first measurements of radiation in an ITER-like configuration are presented.

2. Experimental set-up

To improve the quality of radiation measurements on JET, two new bolometric cameras with horizontal (KB5H) and vertical (KB5V) views of the plasma cross-section have been installed [1], providing a substantial upgrade in capabilities: more viewing chords, higher energy range, higher sensitivity, lower noise and therefore lower detectable signals. Both cameras collect the radiation along 24 chords (48 in total versus 31 channels for old bolometers), eight of which in each case cross the divertor region with 8 cm separation (versus 25 cm separation for old bolometers) between the chord axes (see Fig. 1). The detectors are miniaturised metal foil detectors: an 8 μm-thick gold-absorbing layer on a 20 μm-thick mica substrate and a gold meander on the rear side with a typical resistance

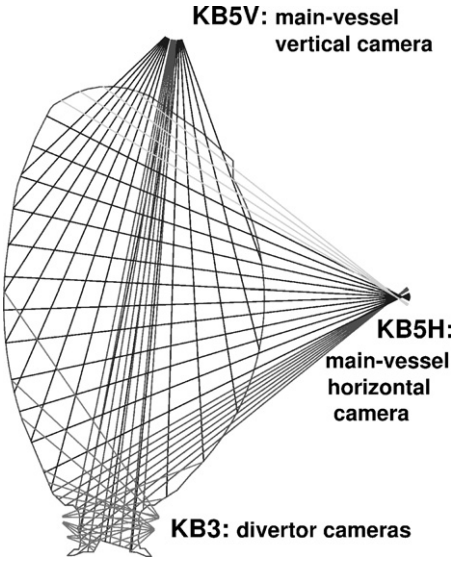

Fig. 1. Lines-of-sight for the vertical and horizontal bolomer cameras as well for the divertor bolometers.

of 1.2 kΩ. The measured sensitivity of the bolometers varies between 3.8 and 6.2 V/W in the absorption range 2.5 eV–10 keV (2.5 eV–5 keV for the old JET bolometers equipped with a 4 μm-thick gold-absorbing layer) with a cooling time constant of about 0.2 s. A 40 V_{pp} sinusoidal voltage at 50 kHz is applied to each bridge of the bolometer separately and the electronics amplifies the output (up to a factor of 5000) with a maximum bandwidth of 2 kHz. Use of synchronous demodulation techniques with a carrier frequency of 50 kHz and an improved shielding concept has permitted a dramatic decrease in the detection limit ($S/N = 1$) to ~2 μW/cm^2 with a bandwidth of $\Delta f = 200$ Hz (versus 70 μW/cm^2 at $\Delta f = 10$ Hz for the old bolometry system).

In addition, three new dedicated divertor bolometers (KB3) with twelve lines-of-sight in total, optimised views and technical improvements have replaced the old ones. The combination of the divertor bolometers with the KB5 overview cameras leads to a substantial improvement in radiation pattern reconstructions, in particular in the divertor region.

Two survey spectrometers (KS3) in the visible provide integrated D_α (656.27 nm), D_β (486.13 nm) and D_γ (434.05 nm) intensities as well as impurity signals (CII (515 nm) and CIII (465 nm)) over both divertor legs. Another spectrometer [2] has 13 spatial tracks across the outer target, each 13 mm wide. It covers the visible spectrum range 415–535 nm, and can monitor the CD-band ($A^2\Delta \rightarrow X^2\Pi$ transition), CII (426.7 nm) and D_γ simultaneously. In addition to the spectroscopic diagnostics, there is a poloidal array of fixed Langmuir probes (LP) in the inner and outer divertor targets that are used to measure local saturation current (I_s), electron density and temperature. The power flux and absorbed energy to plasma-facing surfaces is measured with an infrared camera and thermocouples (TC).

3. Results and discussion

L-mode density limit experiments have been performed with $B_T = 2.4$ T, $I_p = 1.7$ MA in ohmic discharges and in discharges with additional NBI-power of 1.0–1.8 MW. Fig. 2 shows the time evolution of the parameters of an ohmic discharge in JET with the JET MkII-HD divertor in which the inner strike point (ISP) was located on the horizontal plate and the outer one (OSP) on the vertical target (see Fig. 4). The plasma density was raised steadily

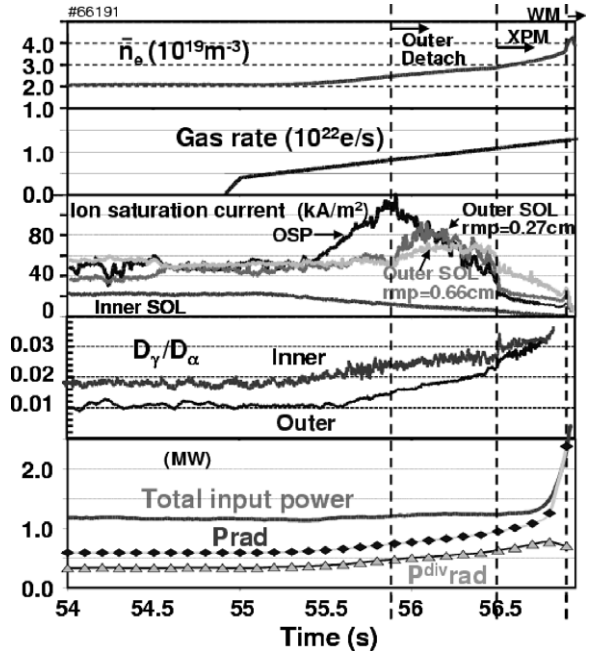

Fig. 2. Time evolution of the parameters of an ohmic discharge in JET with the JET MkII-HD divertor: (a) $\bar{n}_e$, (b) gas rate, (c) I_s of individual Langmuir probes at strike point and in SOL, (d) D_γ/D_α-emission line ratios at the inner and outer targets, and (e) P_{heat}, P_{rad} and P^{div}_{rad}.

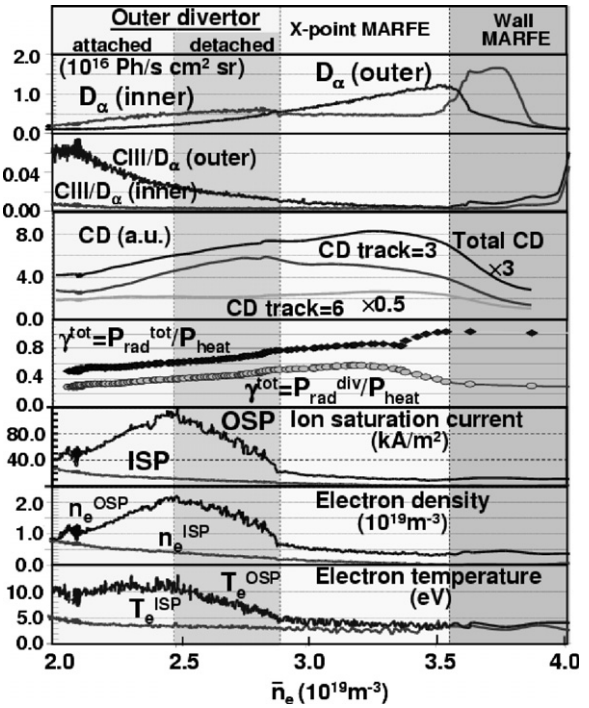

Fig. 3. Characteristics of the MkII-HD divertor plasma as function of $\bar{n}_e$.

to the density limit by gas fuelling into the inner divertor. With continuous deuterium puffing, a high density, low temperature plasma forms inside the separatrix near the X-point. This is the so-called X-point MARFE (XPM). The XPM, which is the precursor to the ultimate density limit, appears at about $\bar{n}_e^{XPM} = 3.0 \times 10^{19}\ m^{-3}$ at a radiative power fraction ($\gamma = P_{rad}/P_{heat}$) of ≈80%. The $\bar{n}_e^{XPM}$ increases with P_{heat}: $\bar{n}_e^{XPM} = 3.3 \times 10^{19}\ m^{-3}$ and $\bar{n}_e^{XPM} = 3.8 \times 10^{19}\ m^{-3}$ for auxiliary heating powers of 1.0 MW and 1.8 MW, respectively.

The ion saturation current in the inner scrape-off layer (I_s^{SOL}) remains initially at a constant level, but falls strongly as the density ramp progresses, indicating that the inner divertor is detached almost immediately. Further evidence for detachment is seen from the inner divertor D_α-emission and the D_γ/D_α-ratio (characteristic of the onset of recombination [3]), both of which continually increase throughout the density ramp (see Fig. 3).

An abrupt reduction in ion current at the outer strike point (I_s^{OSP}) is observed at 55.85 s. Nonetheless, the outer SOL currents continue to increase until 56.1 s and 56.4 s for LPs located on flux surfaces, which map to 1.1 and 4.1 cm from the separatrix at the outer midplane. Detachment thus occurs first at the separatrix and then propagates deeper into the SOL with time. At 56.5 s, the outer divertor completely detaches, thereby triggering the X-Point MARFE formation. This is in good agreement with previous results [4], confirming the general observation that the plasma is stable if at least one of the divertor legs remains attached. Because the inner leg detaches much earlier than the outer, it is the outer divertor which finally determines the density limit.

The line-integrated intensities measured by the bolometer systems are tomographically inverted by an 'anisotropic diffusion model tomography' [5,6]. The tomographically derived P_{rad} increases with density from 50% to 80% of total input power just before the XPM formation. The new bolometers now permit the divertor radiation distribution to be measured with significantly improved spatial resolution, allowing the divertor and main chamber radiation fractions to be clearly resolved. P^{div}_{rad}, shown in Fig. 2, increases with density, reaching a maximum value of ~0.6 P_{heat} just before XPM formation. It drops during the formation of the wall

MARFE (WM). The absorbed energy in the divertor derived from thermocouples ($E_{TC} = 7.6$ MJ) is in good agreement with the total radiated power taking into account the wall load in the divertor due to radiation E_{wall}^{rad}, which is approximately 37% of $P_{rad}(E_{TC} \approx E_{in} - E_{rad} + E_{rad}^{wall})$.

Fig. 3 depicts the time evolution of Fig. 2 as a function of plasma density. The figure is subdivided into four different phases: the attached (1) and detached (2) outer divertor; X-point (3) and wall (4) MARFE phases. The inner divertor is detached during all phases. D_α-emission in the inner leg increases until the XPM forms, then stabilises at a constant level during the XPM phase and finally drastically increases during the wall MARFE formation. In the outer divertor, the D_α-emission continuously increases until the WM formation: in the first phase this occurs because of the rise of ion fluxes into the outer divertor, and during the detached phase as a consequence of the drop in the electron temperature. The ratio of ionisation per photon for D_α, the so-called S/XB-value, decreases by a factor of 2.5 (from 18 ($T_e = 10$ eV, $n_e = 2 \times 10^{19}$ m^{-3}) to 7 ($T_e = 5$ eV, $n_e = 1 \times 10^{19}$ m^{-3}) [7]) during the detached phases, indicating an increase by a factor of 2.5 in the D_α-emission, due to excitation only. A significant reduction of the CIII/D_α-ratio is observed up to the formation of the wall MARFE, corresponding to a decrease of both electron temperature and physical sputtering. The total CD-band emission (integrated over 13 tracks of the KT3B spectrometer) increases up to the formation of the WM. The CD-band emission from the third track (about $d = 13$ mm distance between the line-of-sight and vertical divertor), increases during the attached phase, and also continues to increase during the detached phase. During detachment in the outer divertor, an increase of the neutral pressure in the divertor chamber has been observed. Thermal neutrals and also energetic neutrals (generated by charge-exchange) bombard the divertor wall and could provide significant chemical erosion. In this case, the production of the hydrocarbons is not localised at the strike point and could take place across the entire divertor wall surface. This is one of the possible explanations for the increase of the line-integrated CD-signal.

$\gamma = P_{rad}/P_{heat}$ increases from 0.5 to 0.8 just before the XPM onset. The fraction of power radiated in the divertor ($P_{rad}^{div}/P_{rad}^{tot}$) increases from 0.56 to 0.67 at XPM onset and decreases abruptly during the transition to the WM phase.

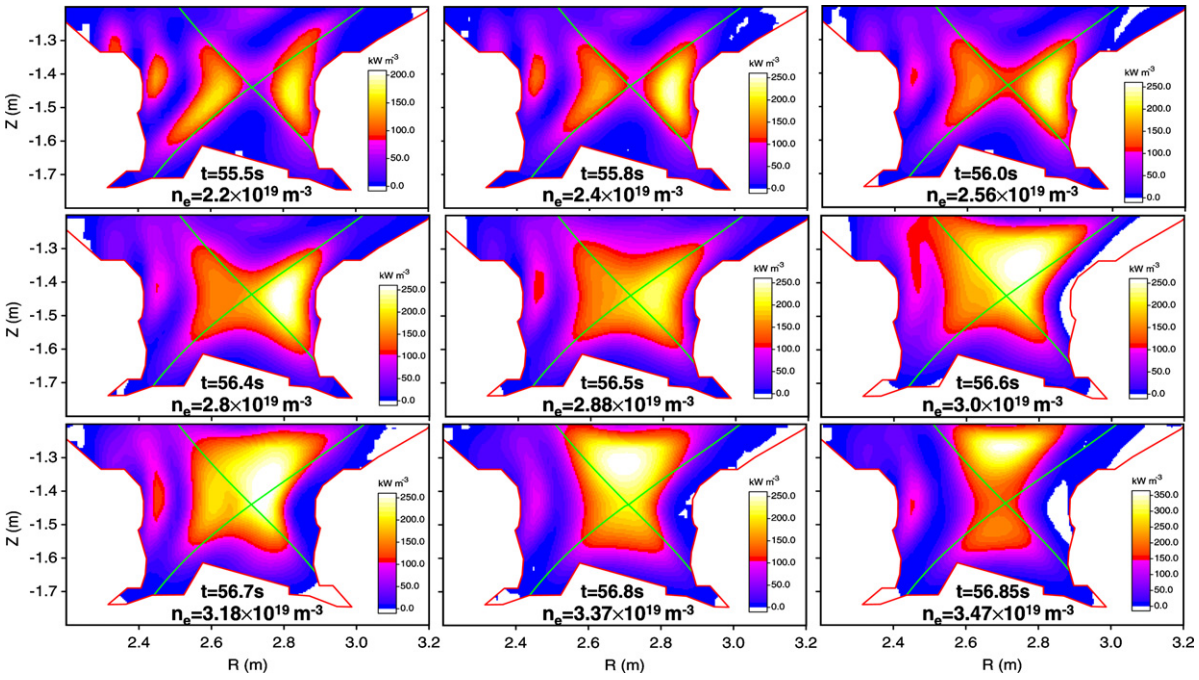

Fig. 4. Tomographic reconstruction of the total radiation in the divertor region at different $\bar{n}_e$ during the density ramp.

Fig. 4 shows the tomographic reconstruction of radiation in the divertor region at 9 different $\bar{n}_e$:

$2.2\times10^{19}\,m^{-3}$ *and* $2.4\times10^{19}\,m^{-3}$: In this early phase, the radiation distribution is essentially symmetric. The plasma radiates mostly from the inner and outer divertor SOL regions. Moderate radiation is observed directly from the X-point region. The outer divertor is attached and the electron temperature at the OSP is about 11 eV.

$2.56\times10^{19}\,m^{-3}$: The total radiation continues to increases in the outer SOL and begins to decrease in the inner SOL. This is the moment at which the OSP starts to detach.

$2.8\times10^{19}\,m^{-3}$ *and* $2.88\times10^{19}\,m^{-3}$: There is a strong in–out asymmetry, with significantly more radiation from the outer divertor leg. An increase of radiation at the X-point and inside the separatrix above the X-point is observed. The saturation current decreases markedly at the OSP and the electron temperature is about 5 eV.

$3.0\times10^{19}\,m^{-3}$: The radiation moves entirely to the X-point, forming an XPM at 80% radiative power fraction. The outer divertor at this time is fully detached. D_α-emission in the outer divertor (see Fig. 3) and the neutral pressure in the divertor chamber (not shown) continue to increase.

$3.18\times10^{19}\,m^{-3}$, $3.37\times10^{19}\,m^{-3}$ *and* $3.47\times10^{19}\,m^{-3}$: the radiation above the X-point increases and finally moves away towards the inner wall. From the formation of the inner wall MARFE just below the level of the magnetic axis, the density limit disruption ensues.

A new operational campaign at JET has recently begun, with first attempts at producing high triangularity $\delta = 0.53$, ITER-like plasma configurations. These discharges are ultimately intended to investigate Type I ELMing H-modes at high input power and plasma current. They are particularly interesting from the divertor physics point of view with regard to the rather short inner divertor leg and the consequent proximity of the X-point to the inner divertor target.

Fig. 5 shows the reconstructed radiation in an inter-ELM period (averaged over 10 ms) and during an ELM (averaged over ELMs) in a discharge with $B_T = 2.7$ T, $I_p = 2.5$ MA, 14.5 MW NBI and 2.5 MW ICRH power, $q_{95} = 3.6$, $\bar{n}_e/n_{GW} = 0.87$. The ELM frequency was 30–35 Hz. Between ELMs the majority of the radiation is located at the X-point and at the ISP, as well in the outer SOL. At the inner strike point $T_e \sim 43$ eV and the inner divertor is attached. P_{rad} (averaged over 10 ms in the inter-ELM period) is 7.75 MW (46% of P_{heat})

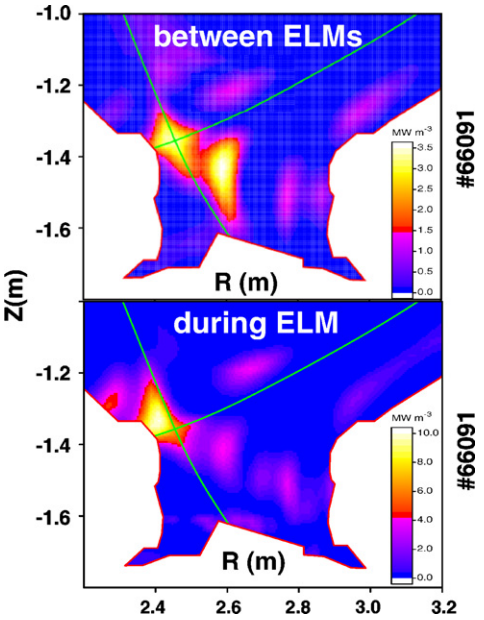

Fig. 5. Total radiation distribution between ELMs (top) and during an ELM in a discharge with an ITER-like configuration.

and the wall load in the divertor due to this radiation is ≈30% of P_{rad}. We find that the radiation during an ELM is mainly located in the inner divertor. The total radiated energy during the ELM, evaluated by an algorithm similar to [8], is 40–50 kJ, which corresponds to 20% of ELM-energy losses ($\Delta W_{dia}^{ELM} \approx 240$ kJ.)

The EDGE2D-simulation of discharges at high P_{heat} and density [9] predicts a strong contribution of atomic processes (line emissions, charge-exchange) to volumetric power losses. The simulated out–in target power asymmetry is $P_T^{outer}/P_T^{inner} \approx 2.5$, agrees well with the result from thermocouples ($P_T^{outer}/P_T^{inner} \approx 2.2$).

4. Summary and conclusion

The new bolometer system provides measurements with significantly improved spatial resolution, allowing the divertor and main chamber radiation fractions to be clearly resolved.

Significant differences in the radiation distribution have been observed during density ramp-up experiments. In the early phase (outer divertor still attached) the distribution is nearly symmetric with respect to the inner and outer divertors. It becomes strongly asymmetric in the phase with a detached outer divertor: considerably more radiation in the

outer leg and noticeable radiation at the X-point. It is this outer divertor detachment which triggers the X-Point MARFE formation. The radiation power fraction $\gamma = P_{\mathrm{rad}}/P_{\mathrm{heat}}$ increases from 0.5 to 0.8 just before the XPM onset. The $P_{\mathrm{rad}}^{\mathrm{div}}/P_{\mathrm{rad}}^{\mathrm{tot}}$ fraction varies between 0.56 and 0.67. The absorbed energy in the divertor derived from thermocouples is in good agreement with the total radiated power taking into account the wall load in the divertor due to radiation $E_{\mathrm{wall}}^{\mathrm{rad}}$. The latter was derived from tomographical reconstructions and is approximately 37% of P_{rad}. The D_α-emission shows a strong in–out asymmetry at low density, with more radiation from the inner leg than from the outer. When both legs are detached, the D_α-emission is nearly symmetrical.

The first tomographic reconstructions of total radiation in discharges with an ITER-like magnetic field configuration have been started. Between ELMs a significant part of the radiation is located at the XP and at the ISP as well as in the outer SOL. During ELMs the radiation is located mainly in the inner divertor. About 20% of the ELM-energy losses are radiative.

References

[1] K. McCormick, A. Huber, C. Ingesson, et al., Fus. Eng. Des. 74 (2005) 679.
[2] A.G. Meigs, W. Fundamenski, C. Jupen, et al., in: 27th EPS Conference on Contr. Fusion and Plasma Phys., Budapest, 24B (2000) 1264.
[3] G.M. McCracken, M.F. Stamp, R.D. Monk, et al., J. Nucl. Mater. 38 (1998) 619.
[4] A. Huber, J. Rapp, P. Andrew, et al., J. Nucl. Mater. 337–339 (2005) 241.
[5] L.C. Ingesson, B. Alper, H. Chen, et al., Nucl. Fus. 38 (1998) 1675.
[6] J.C. Fuchs, K.F. Mast, A. Hermann, in: 21st EPS Conference on Contr. Fusion and Plasma Phys., Montpellier, 18B (1994) 1308.
[7] adas.phys.strath.ac.uk.
[8] J.C. Fuchs, T. Eich, A. Hermann, et al., J. Nucl. Mater. 337–339 (2005) 756.
[9] K. Erents et al., J. Nucl. Mater., these Proccedings, doi:10.1016/j.jnucmat.2006.12.066.